Sager, C., Airo, A., Arens, F. L., Rabethge, C., Schulze-Makuch, D. (2020): New types of boulder accumulations in the hyper-arid Atacama Desert. - *Geomorphology*, *350*.

DOI: http://doi.org/10.1016/j.geomorph.2019.106897

Geomorphology 350 (2020) 106897

Contents lists available at ScienceDirect

Geomorphology

journal homepage: www.elsevier.com/locate/geomorph

New types of boulder accumulations in the hyper-arid Atacama Desert

Christof Sager[a,*], Alessandro Airo[a], Felix L. Arens[a], Carolin Rabethge[b], Dirk Schulze-Makuch[a,c,d,e]

[a] Zentrum für Astronomie and Astrophysik, Technische Universität Berlin, Germany
[b] Institute of Geological Sciences, Freie Universität Berlin, Germany
[c] Leibniz-Institute of Freshwater Ecology and Inland Fisheries (IGB), Department of Experimental Limnology, Stechlin, Germany
[d] GFZ German Research Centre for Geoscience, Section Geomicrobiology, Potsdam, Germany
[e] School of the Environment, Washington State University, Pullman, Washington, USA

ARTICLE INFO

Article history:
Received 30 April 2019
Received in revised form 7 October 2019
Accepted 7 October 2019
Available online 28 October 2019

Keywords:
Hyper-arid Atacama Desert
Boulder
Seismic
Mars

ABSTRACT

The accumulation of thousands of boulder-sized clasts into boulder fields in the Atacama Desert has been linked to seismic-driven downslope transport, a rare sedimentary process corroborated by this study. We surveyed boulder arrangements occurring in the Atacama Desert and identified three accumulation types for further investigation: a small circular boulder cluster (BC), a long channelized boulder stream (BS), and a wide convex-shaped boulder field (BF). Drone-based photogrammetric techniques and field observations were used to generate high-quality digital elevation models and orthophotos to determine boulder count, size, coverage, orientation, lithology and local topography. Our data shows that the arrangement of boulder accumulations corresponds with the shape of the accommodation space and the boulder input, where BCs occur at the center of completely confined topographic depressions, BSs occur along laterally confined and incised hill slopes with boulders stacked above each other, and BFs occur on largely unconfined shallow and low-relief slopes with a distinct boulder front. A general downslope increase of average boulder size and coverage was measured in all boulder accumulations and a long-axis orientation of boulders parallel to the transport direction was observed for the BS. Based on these results and the lack of fluvial transport indicators, we conclude that transport and arrangement of boulder accumulations are largely controlled by the interplay of topography and seismic-driven boulder transport, resulting in unique landscape features present in the hyper-arid Atacama Desert. Such sedimentary transport processes are rare on Earth but potentially play a greater role on other arid planetary surfaces that are covered by boulders and subject to sufficient seismic activity.

1. Introduction

Terrestrial boulder accumulations are known to form by multiple processes such as weathering and frost wedging of bedrock forming autochthonous blockfields (Ballantyne, 2010), tsunami events (Maouche et al., 2009; Biolchi et al., 2016; Cox et al., 2018), large landslides (Dai et al., 2018) or through glacier movement (Rose, 1992). Extraterrestrial boulder accumulations have been observed on the hyper-arid and cold Mars, however, their formation processes, such as boulder sorting along thermal contraction crack polygons, remain highly debated (Orloff et al., 2013). The little-studied boulder accumulations in the hyper-arid Atacama Desert, are located in one of the driest and oldest deserts on Earth (Quade et al., 2012; Matmon et al., 2015). Besides infrequent rainfall, the high abundances of rare salts (e.g., nitrates and perchlorates) and the high seismic activity belong to the desert's characteristic features. Previous work has shown that large seismic events trigger the downslope transport of large clasts around the El Buitre area and the Yungay area (Socompa Road) in the Atacama Desert, also effecting the landscape evolution, with regards to bedrock weathering and erosion (Quade et al., 2012; Matmon et al., 2015). Granitoid boulders emerge as resistant corestones from the bedrock on crests or hillslopes and slide or bounce downslope through discrete movement events during seismic shaking. Boulders accumulate and bundle in the plains and at the foot of the hills, forming frequently distinct polished midsections by mutual rubbing during seismic events. Apart from seismic rubbing, boulders seem to experience only minor erosion, making them long-exposed surface features, which is supported by individual boulder exposure ages of > 12 Ma (Matmon et al., 2015). Previous studies also

* Corresponding author.
E-mail address: christof.sager@tu-berlin.de (C. Sager).

https://doi.org/10.1016/j.geomorph.2019.106897

considered aeolian, fluvial, glacial and salt heave processes being responsible for boulder movement and polishing (Quade et al., 2012). However, wind as a transport mechanism was excluded, since gusting winds of at least 100–170 m/s are necessary to move boulders weighing 0.5–0.8 tons (Quade et al., 2012). Taken into consideration the scarcity of surface water, the desert's millions of years existence and boulder polishing being restricted to their mid-sections, fluvial or glacial transport appears unlikely. Although salt heave as a boulder transport mechanism cannot be excluded, the occurrence of smooth and unbroken soil surfaces between boulders contradicts active salt erosion (Quade et al., 2012). We here present a characterization of a variety of boulder accumulation types in the Yungay area, ~90 km southwest of the El Buitre area, advancing our understanding of their formation processes, in the context of the local topography and thus, landscape evolution in the hyper-arid Atacama Desert.

2. Regional setting

The study site selection was preceded by field reconnaissance and satellite imagery survey of boulder accumulations in the northern mountains of the Yungay area, ~60 km southeast of Antofagasta (Fig. 1). The Yungay area receives less than 1 mm/yr precipitation (Rundel et al., 1991; McKay et al., 2003), resulting in erosion rates that are close to zero and boulders having exposure ages of multiple millions of years (Placzek et al., 2014). We identified three distinct types of boulder accumulations as study sites: multiple small circular boulder clusters (BCs), a long channelized boulder stream (BS), and a broad convex-shaped boulder field (BF). Among the range of boulder accumulation morphologies observed in the Yungay area, we chose for this study those examples that best exemplify a particular morphology, although additional boulder accumulation types could be defined. The area is characterized by smooth rounded hills with locally outcropping quartz monzodioritic bedrock, intersected by partly exposed dioritic dikes, as well as adjoining alluvial fans passing over into the valley floors. Small rills and gullies are visible on hill slopes, indicating minimal surface runoff. The region lacks vascular plants but is covered by varnished pebbles, cobbles and boulders. A dense and coherent desert pavement is largely absent. Playas and salars developed in the lowest parts of the valley containing fine-grained sediments and salts.

3. Methods

For depicting morphologic characteristics of five boulder accumulations (three BCs, BF and BS) we used the "Structure-from-Motion" photogrammetry technique to reconstruct the 3D-geometry of a terrain using matching features on overlapping drone-based aerial 2D-images (Westoby et al., 2012). Low altitude images (3–60 m above ground level) were acquired using the camera of a *DJI Phantom 4* with a down-facing camera orientation (pitch 0°) and parallel flight paths for the BF and the BS, while BCs were mapped in 360° flight path around the object with an inclined camera (pitch ~50°). For scaling the BC1 and the BF coded markers were evenly distributed within the study site. The distances and relative height differences between the markers were measured using a laser rangefinder with leveling function mounted on a tripod. Besides the markers that function as scale bars for 3D

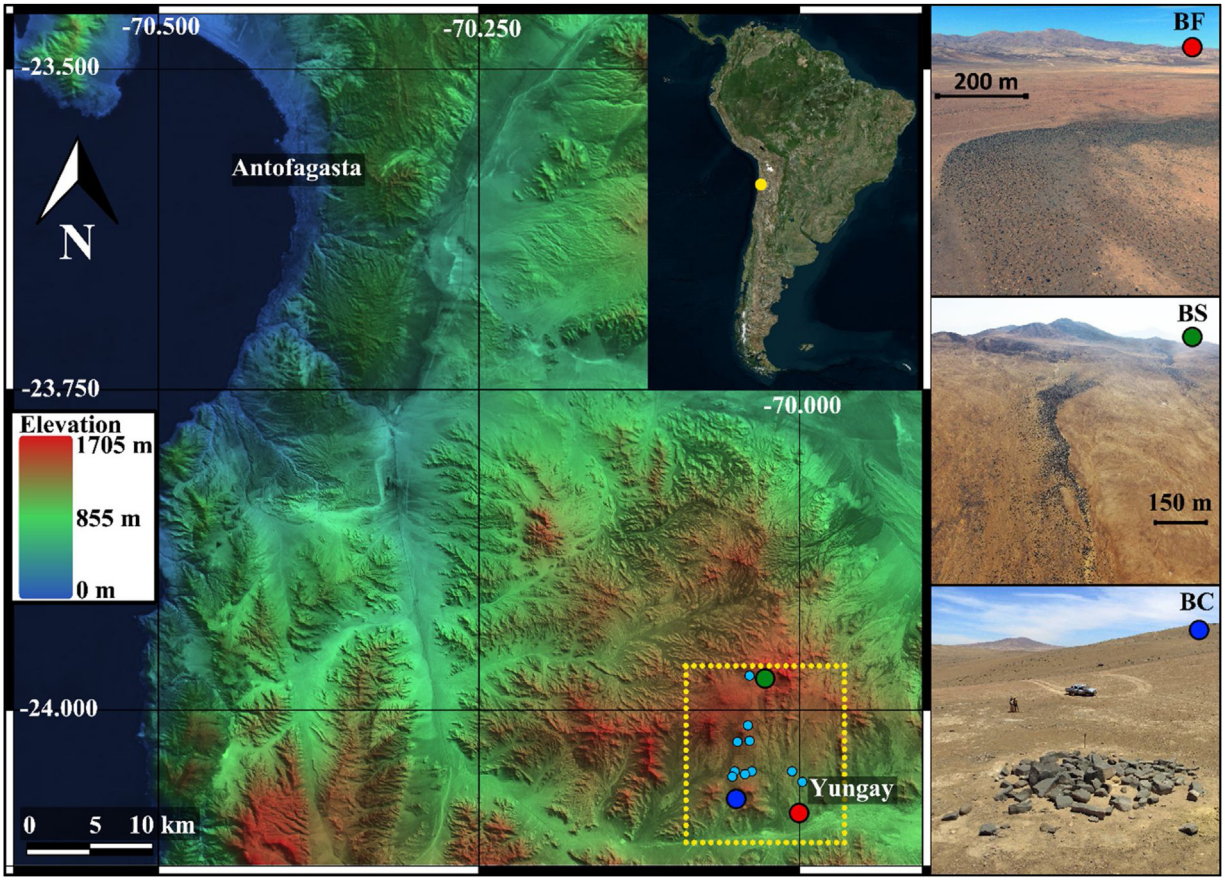

Fig. 1. Geomorphic location map of the study sites. The yellow dot and frame outline the surveyed area in which the investigated BC (blue dot), BF (red dot), BS (green dot) are located, including the additional BCs (light blue dots) that were observed. Location map is based on Aster digital elevation model (DEM) from U.S. Geological Survey and satellite image from Bing maps, 2019 Microsoft.

reconstruction, up to six 1 m plastic tubes have been laid out for the BC1 and the BF transect as check scale bars. The BS and the two additional BCs were scaled based on camera positions and no markers were used. *Agisoft Metashape* was used for photogrammetric reconstructions and 3D-spatial data generation (Agisoft, 2019). A total of seven 3D models were generated. One model was created for each, the BC1 and the BS. For the BF, three models were generated, one overview large-scale model, while the boulder front and the transect were reconstructed at smaller scales. Models for two additional BCs (BC10 and BC11) were generated. Processing reports of the respective 3D models, containing relevant parameters (number of photos, resolutions of orthophotos and DEMs) and errors (e.g., reprojection error) are available as Supplementary Data (see Supplementary material #2a - #2 g). In order to convert the measured relative height differences between the markers into absolute heights for the respective 3D models, the estimated elevation of one marker was defined to be correct and the measured height differences in the field were then subtracted or added to the remaining markers and thereby, improve the tilt and vertical accuracy of the model. The altitude estimation is based on the drone's GPS coordinates, stored in the image data during flight or in a handheld GPS device for the BS. High-resolution digital elevation models (DEMs) and geometrically corrected aerial images (orthophotos) of the BCs, the BF and the BS were generated in Agisoft Metashape. The 1 m long check scale bars showed lengths ranging from 99 to 101 cm in the respective orthophotos of the BC1 and the BF transect. The orthophotos exported as .tif files were mapped by hand in Adobe Photoshop CS5.1. Thereby, the entire visible boulder area in the orthographic view was mapped, which often contrasts dark from the bright ground. The GIS application *QGIS* was used to create maps in which the DEMs and orthophotos are displayed (QGIS Development Team, 2019). Hand-mapped orthophotos were converted to binary images of similar resolution with the image analysis software *FIJI* and boulder size, count and coverage were measured with the *Biovoxxel* plugin (Schindelin et al., 2012; Brocher, 2015). The orientation was measured using the *Ellipse Split* plugin, which applies a fitting ellipse to each particle and measures its long-axis orientation (Wagner and Eglinger, 2017). The orientation of boulders with an aspect ratio larger than 1.2 was plotted with *GeoRose* (Yong Technology Inc., 2014). Detailed investigations were carried out for the shown BC1, two additional BCs and multiple subareas of the BF as well as the BS. Only clasts with a visible surface area larger than 0.067 m^2 (corresponding to a 26 × 26 cm square) were considered for boulder analysis. Boulder coverage is defined as the percentage of boulders covering a certain surface area. Boulder count refers to the number of boulders within a specified area. For coverage analysis, the BCs were divided into three concentric rings with their center being based on the pixel-weighted center of mass of the mapped orthophoto. The BC11 was divided into four rings. Boulders located within two rings were assigned to the ring containing the larger fraction of the boulder surface area. A 180 × 15 m transect of the BF was divided into 12 subareas (15 × 15 m) and two additional sub-areas were defined for boulder orientation along the boulder front, while five subareas (15 × 15 m) along the BS were defined for analysis. For boulder size, count and orientation analysis, boulders located within two subareas were assigned to the ring or 15 × 15 m square containing the larger fraction of the boulder surface resulting in adjusted rings and adjusted 15 × 15 m subareas (Fig. 2a, b). To estimate the average elevation of a sampling area, the average of the four corner points of a sampling area for the BS and BF was used. The elevation estimation for the BC1 is based on the height of three points located on boulder free area in the middle of the three rings. A hand mapping error of four pixels was assumed for the BCs and BF, as well as 2 pixels for the BS. Thereby each particle was dilated and eroded by one or two pixels. The measurements for boulder size, median and coverage were repeated and subtracted from the original values to calculate the error bars included in the results.

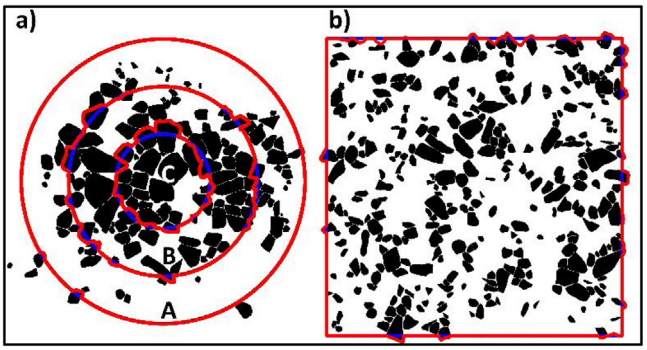

Fig. 2. Mapping methodology. a) Binary image of the BC1 divided into concentric rings (blue) and adjusted rings (red) (A-outer, B-middle, C-inner ring). b) The BF and the BS were divided into 15 × 15 m subareas (blue) for coverage analysis and adjusted subareas (red) for grain size and orientation analysis.

4. Results

Boulders located within the study area either originate from quartz monzodioritic bedrock or intersecting dioritic dikes outcropping on slopes and hillcrests. While the quartz monzodioritic bedrock commonly emerges as onion-weathered sub-round corestones, the dioritic dikes frequently protrude up to one meter above the soil surface as angular blocks (Fig. 3a, b). Outcropping rocks are intensely coated by desert varnish but lack rubbing surfaces (Fig. 3a, b). As a general downslope trend for all investigated boulder accumulations we measured an increase of boulder coverage and average size while the boulder shapes become overall more rounded and smoothened; frequently showing multiple generations of rubbing surfaces along their midsections (Fig. 4 and Supplementary material #1). Similar to the downslope increase of the average size, the boulder median size increases as well due to a reduction of the smallest boulders and an increase of the relative amount of the largest boulders. Additionally, in contrast to the more erosion resistant diorites, the quartz monzodiorites weather readily into grus. With increasing boulder coverage the top few centimeters of soil become dominated by loose silt to coarse sand in which the boulders are embedded (Fig. 3c, d). Where boulder coverage is low (<4 %), the surface soil surrounding scattered boulders is identical to boulder-free areas. However, none of the surveyed boulders, ranging from their source to the boulder accumulations, were observed to be buried and are generally only submerged a few centimeters within the surface soil. Besides occasional small rills and gullies on hill slopes, no further indications for fluvial transport, such as recently active riverbeds, scour marks around boulders, nor boulder imbrication have been observed. All three studied boulder accumulations have shapes that correspond to the topography of their accommodation space (Fig. 5 and Supplementary material #1). The circular BC1, containing 125 boulders of mainly dioritic lithology, is located at ~1208 m elevation around the center of a very shallow bowl-shaped and circular depression with a slope of ~0.9° and ~12 m in diameter (Fig. 5a). While only few boulders enter this fully confined accommodation space due to the small catchment area, the boulder coverage and average size increase abruptly towards the center of the depression reaching 71.8 % (Fig. 4a). These densely packed boulders show multiple extensive midsection rubbing-surfaces and frequent boulder-to-boulder contacts with several boulders that imprinted themselves into each other. A preferred orientation of boulders within BC1 is not observed (Fig. 5a'). The loose grus layer is bedded horizontally and pebble-to-cobble-sized clasts are largely absent between the

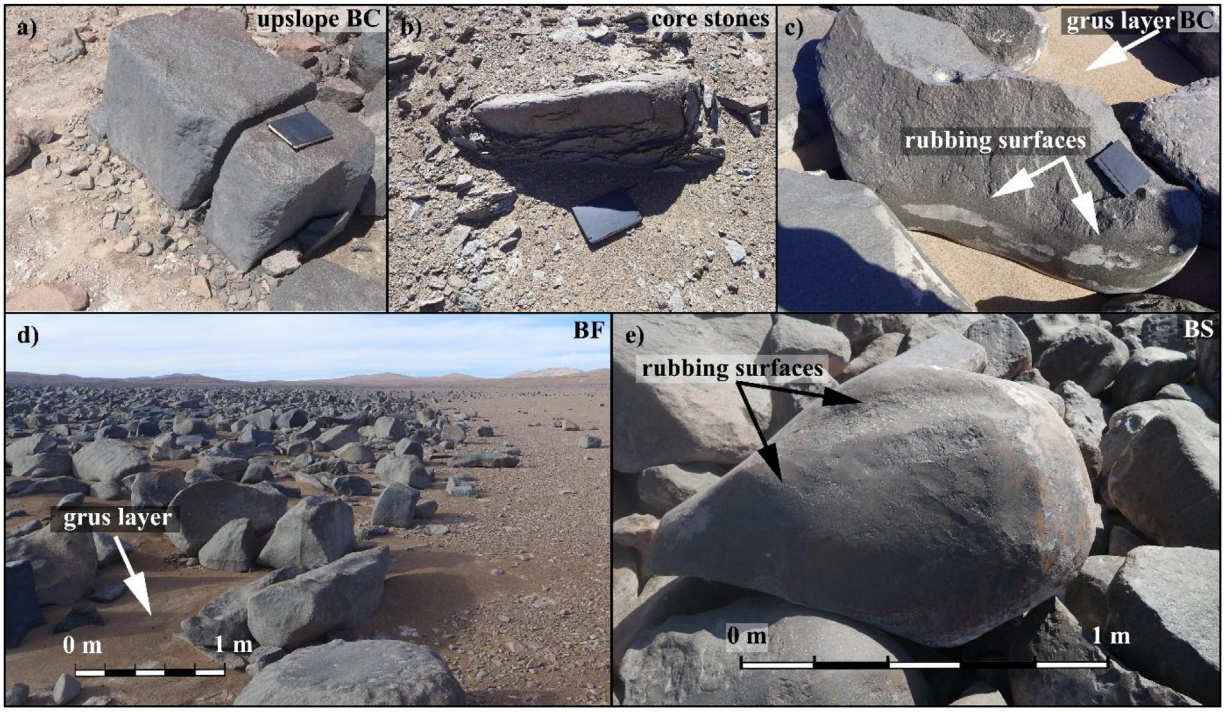

Fig. 3. Photographs of boulder accumulations in the study sites. a) Angular dioritic boulders originating upslope of the BC1 from an outcropping dioritic dike. b) Core stones weathering out of the quartz monzodioritic bedrock. c) Rounded and polished boulder midsections of the BC1 with grus between them. d) The convex-shaped boulder front of the BF with the visible grus layer present between boulders being absent outside the boulder front. e) Stacked boulders in the BS showing rubbing surfaces on all sides.

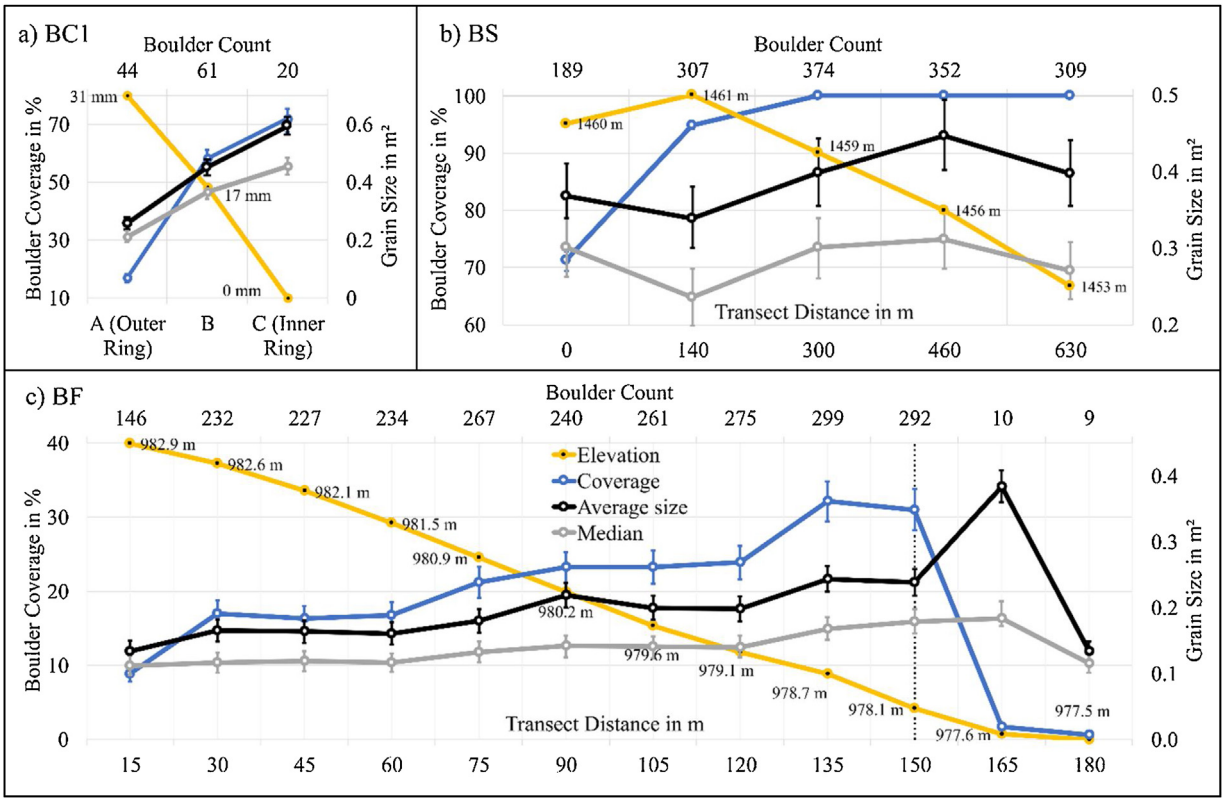

Fig. 4. Boulder accumulation downslope trends showing boulder count, transect distance, coverage (blue), average size (black), median size (grey) and elevation (yellow, the lowest elevation in the Depression of BC1 was set to 0 mm). a) The downslope trend of BC1. b) The downslope trend of BS. c) The downslope trend of BF with the boulder field margin at 150 m (dotted line).

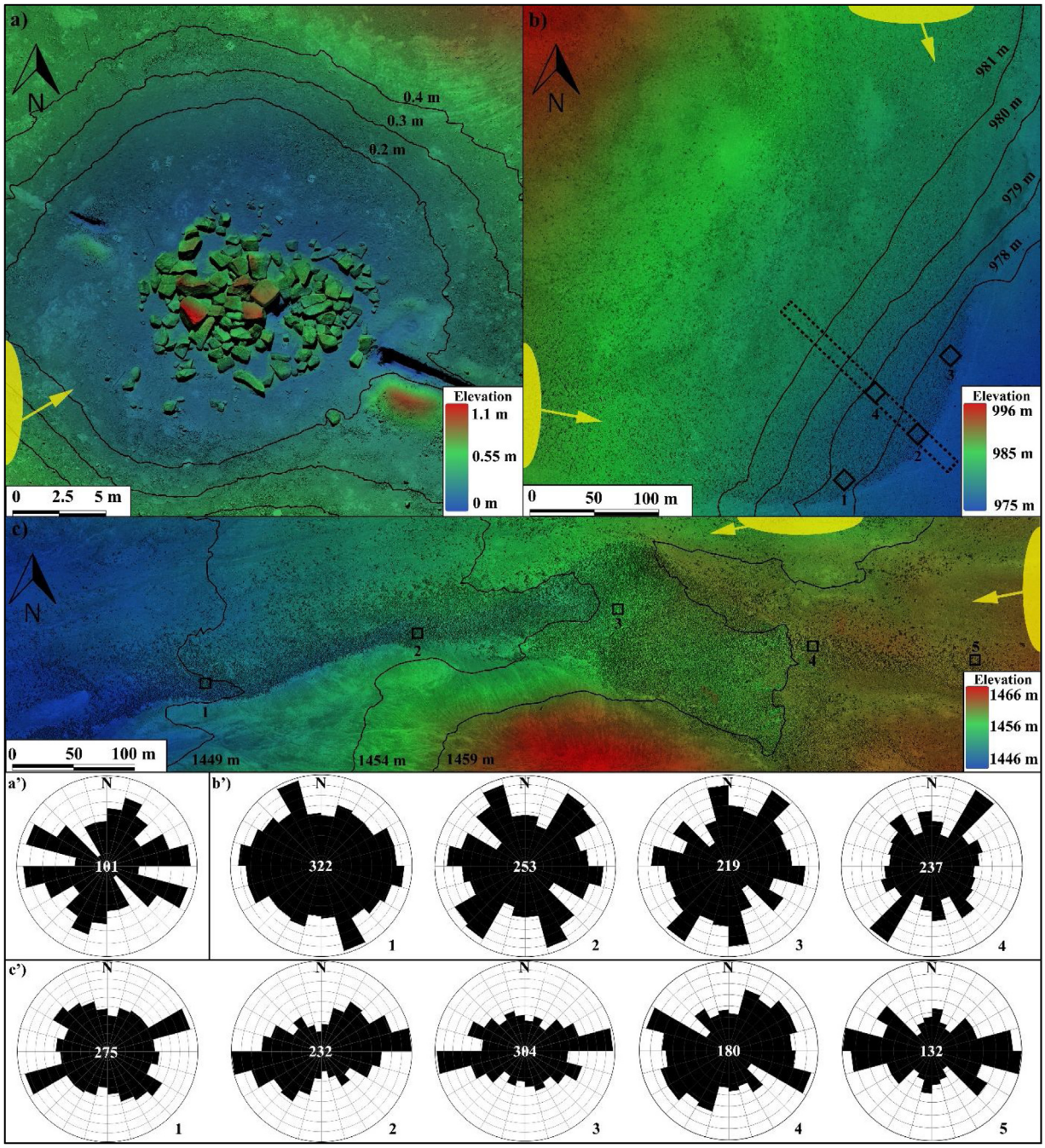

Fig. 5. Boulder accumulations are shown in combined color-coded DEM and orthophoto view with labeled contour lines (black). Subareas of the BF and BS (black frames) correspond to the labeled rose diagrams. The boulder source areas are not within the depicted area, however, the direction to main source areas and the transport paths are shown in yellow. a) The BC1 is located within a fully confined topographic depression at ~1208 m elevation, but the lowest point of the DEM is set to 0 m b) The BF is located on an unconfined low-relief slope. The transect (large dotted frame) is 180 m long. c) The BS is located within a confined morphology of a dry riverbed. a')b')c') Rose diagrams showing boulder orientation indicated by black bars (N = north). A larger bar radius corresponds to a higher number of boulders orientated in the respective direction. The white number shows the amount of surveyed boulders.

boulders (Fig. 3c). The BF, containing tens of thousands of boulders, originating upslope from extensive outcrops and terminating sharply with a convex-shaped front, is located on a northwest-to-southeast oriented low gradient slope of ~2.0° with no downslope topographic confinement (Fig. 5b). Whereas the BF described in this study exhibits a highly distinct front (Fig. 3d), other BFs in the Yungay area were observed to show a range of morphologies, up to highly defuse boulder fronts grading into scattered boulder fields. The boulder coverage along a 15 × 180 m transect shows a downslope increase from 8.9 to 31.0 % and dropping to 1.6 % beyond the boulder front (Fig. 4c). The DEM shows that the BF is located on a low relief morphology while the slope decreases to ~0.45° at the boulder front. Although the BF is located on a largely flat terrain, the center of the convex boulder front which is most advanced downhill is slightly lowered (area between subarea 1 and 3 in Fig. 5b) in relation to the marginal areas of the boulder front. Thus, the boulders that are most advanced are currently at the lowest point within the occupied migration path. Few boulders are in direct contact with each other and rubbing surfaces are less frequent and observed to be more varnished compared to those in BCs. Elongated boulders of

the subareas 1 and 4 show a preferred orientation, not observed at subareas 2 and 3 (Fig. 5b'). The BS, containing thousands of boulders, is located on a west-to-east oriented slope, incised by an apparently inactive fluvial channel with a slope of ~1.0° in which the majority of boulders have accumulated (Fig. 5c). The extensive source area of boulders to the east and northeast causing a high boulder input in combination with the laterally confined accommodation space with channel slopes greater than 5.0° results in very high coverage along the former thalweg exceeding 100% for some subareas with boulders being stacked on top of each other (Fig. 4b). Only boulders in the BS show polished rubbing surfaces on all sides, especially those that are stacked (Fig. 3e). Boulders located in the thalweg show a clear orientation of their long-axis parallel to the thalweg (Fig. 5c').

5. Discussion and conclusion

Our field observations and measurements show no indication for fluvially-driven boulder movement, supporting a seismic-driven downslope transport mechanism as proposed by Quade et al. (2012); Matmon et al. (2012, 2015). Besides the lack of scour marks around boulders or their imbrication, none of the thousands of large boulders observed were even partially submerged as would be expected for fluvial transport, whereas seismic-induced particle-size segregation would prevent boulder burial, as known from kinetic sieving models where larger particles are leveled upwards (Rosato et al., 1987). The correlation between the increase of mid-section rubbing surfaces and boulder coverage supports a seismic shaking mechanism in which the boulders rotate horizontally and shake laterally without rolling, as it would be otherwise the case for fluvial bed-load transport. Furthermore, the downslope orientation of the boulder long-axis supports a sliding mechanism and not a downhill rolling mechanism where the boulder's long-axis would be expected to largely have a perpendicular orientation (Fig. 5c'). These findings are in accordance with in situ exposure dating results from individual boulders of the Yungay area (Socompa Road) and the El Buitre boulder field indicating no boulder turnover for millions of years (Matmon et al., 2015). Furthermore, the downslope increase in the average boulders size and coverage corroborate previous findings by Quade et al. (2012), which suggested that this trend is due to larger granodioritic boulders undergoing only minor erosion during seismic-driven transport, while the smaller granodioritic boulders disintegrate due to collisional spallation with the larger boulders into grus (Fig. 4). We observe similar boulder degradation for the quartz monzodioritic boulders whereas we found little to no indication for this erosion process for the dioritic boulders. Although we cannot exclude such a spallation-induced grain-size sorting mechanism for the dioritic boulders, we propose, that, inverse to fluvial transport but analogous to dry grain flow in colluvial fans, larger boulder advance more rapidly downslope during seismic-driven transport (Blikra and Nemec, 1998). Based on our results we conclude that the downslope transport paths and the shape of boulder accumulations is controlled by the topography of the accommodation space, where circular BCs occur at the center of fully-confined topographic depressions, BSs occur along incised hill slopes with lateral confinement, and BFs occur on largely unconfined low-relief slopes (Fig. 5). In addition to the accommodation space, the degree of boulder input controls the extent of the boulder accumulation and its boulder coverage, since a large number of boulders is likely to result in higher coverage and a larger extent than a small number of boulders within a particular accommodation space, such as an incised hill slope. In contrast to most other BFs we observed in the area, which lack a discrete front and transitioning into scattered boulder fields of lower coverage, the BF investigated here exhibits a sharp front, which we propose to originate from the high boulder input and the slope reduction resulting in a reduced downslope transport and thus boulder damming. The convex shape of the front presumably results from the slightly lower elevation at the center of the boulder front. Although we observe a damming of boulders, their coverage does not exceed 27%, which could be limited by boulder collision-induced dispersion during earthquake events (Fig. 4c). Such a collision-driven transport of boulders could result in the migration of boulders into horizontal terrain if a continuous influx of upslope boulders is provided. If, however, the boulder input is high and the accommodation space is laterally confined, as the case for the BS, boulder coverage can even exceed 100% resulting in stacked boulders (Figs. 3e, 4 b). During seismic events these stacked boulders weighing several tons are assumed to rotate, which is indicated by extensive rubbing surfaces occurring on all sides (Fig. 3e). The here newly described BCs show in their center boulder coverages exceeding 50% (Fig. 4a and Supplementary material #1). We interpret this high coverage to result from their fully confined topography, while boulder stacking does not occur due to the shallow slope. In contrast to the BF and BS, which we assume to still propagate downslope and change their shape, we suggest the BCs to be more stable in shape and position since they are already located at the lowest point of a circular depression. An increased boulder input to the BC1 would presumably result in a higher boulder coverage, but only in a minor BC-size increase, because an ongoing increase in size would entail boulders being transported further downslope at the south-eastern margin of the depression, where only a shallow topographic barrier is located. This is corroborated by the observation of polished boulders located further downslope of the BC1. Boulder accumulations with their relatively low transport rates, located in a hyper-arid environment represent a rare setting on Earth, while at various locations on Mars numerous boulder accumulations have been discovered (e.g., Grant et al., 2006; Levy et al., 2008; Küppers et al., 2014). Multiple formation scenarios have been proposed for the different types of boulder accumulations found on Mars, such as (1) 'Boulder halos' being circular boulder arrangements that are assumed to be created by impact ejecta (Levy et al., 2018), (2) 'Rubble piles' that are regularly spaced boulder accumulations (20–35 m) sitting on local high grounds for which their formation has been linked to thermal contraction and rock sorting on polygonated grounds (Mellon et al., 2008), or (3) 'Boulder clustering' along polygon margins, which has been proposed to result from a boulder transport mechanism driven by seasonal CO_2 frost formation and sublimation cycles (Orloff et al., 2013). Some boulder fields on Mars show morphological similarities to the here studied BF, such as the distinct transition from the densely covered terrain to the smooth terrain lacking boulders (Fig. 6). However, for none of the boulder accumulations on Mars a topography-controlled and seismic-driven formation mechanism has been proposed although many analogies between Mars and the Atacama Desert exist, such as the long-term hyper-aridity (Hartley et al., 2005; Amundson et al., 2012). Hence, the Atacama Desert soils are frequently used as an analog to the Martian regolith (Warren-Rhodes et al., 2019). Although a similarity between some morphological attributes of boulder accumulations in the Atacama Desert and on Mars exists, it cannot be concluded that they have a similar formation process. Hence, to our knowledge, the formation of the studied boulder accumulations in the Atacama Desert remains unique to Earth but could occur on other dry planetary surfaces that are covered by boulders and are subject to sufficient seismic activity.

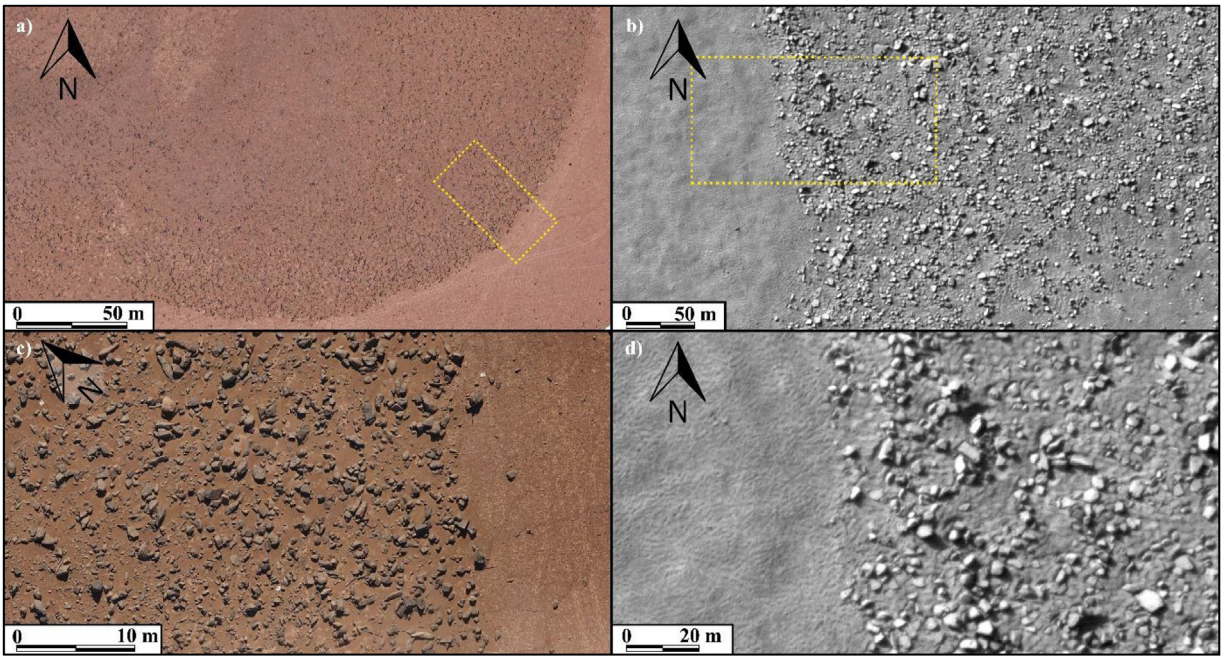

Fig. 6. Contact between a boulder field with smooth and flat terrain in the (a) Atacama Desert and on (b) Mars, HiRISE image ESP_024117_1185 (latitude: -61.339° centered, longitude: 100.730° east) (NASA/JPL/University of Arizona, 2011). c) Enlarged area of the BF (yellow frame in a). d) Enlarged area of a Martian boulder field (yellow frame in b).

Declaration of Competing Interest

The authors declare that they have no known competing financial interests or personal relationships that could have appeared to influence the work reported in this paper.

Acknowledgements

We thank J. Meyer, J. Hulin, L. Jentzsch, M. Homann and A. Bernhardt for their support and discussions during the project. We also acknowledge support by the ERC Advanced Grant Habitability of Martian Environments: Exploring the Physiological and Environmental Limits of Life (# 339231).

Appendix A. Supplementary data

Supplementary material related to this article can be found, in the online version, at doi:https://doi.org/10.1016/j.geomorph.2019.106897.

References

Agisoft, 2019. Metashape.
Amundson, R., Dietrich, W., Bellugi, D., Ewing, S., Nishiizumi, K., Chong, G., Owen, J., Finkel, R., Heimsath, A., Stewart, B., Caffee, M., 2012. Geomorphologic evidence for the late Pliocene onset of hyperaridity in the Atacama Desert. J. Geophys. Res. 124, 1048–1070.
Ballantyne, C.K., 2010. A general model of autochthonous blockfield evolution. Permafr. Periglac. Process. 21, 289–300.
Biolchi, S., Furlani, S., Antonioli, F., Baldassini, N., Causon Deguara, J., Devoto, S., Di Stefano, A., Evans, J., Gambin, T., Gauci, R., Mastronuzzi, G., Monaco, C., Scicchitano, G., 2016. Boulder accumulations related to extreme wave events on the eastern coast of Malta. Nat. Hazards Earth Syst. Sci. 16, 737–756.
Blikra, L.H., Nemec, W., 1998. Postglacial colluvium in western Norway: depositional processes, facies and palaeoclimatic record. Sedimentology 45, 909–959.
Brocher J., 2015. The BioVoxxel Image Processing and Analysis Toolbox.
Cox, R., Jahn, K.L., Watkins, O.G., Cox, P., 2018. Extraordinary boulder transport by storm waves (west of Ireland, winter 2013–2014), and criteria for analysing coastal boulder deposits. Earth. Rev. 177, 623–636.
Dai, Z., Wang, F., Cheng, Q., 2018. Deposit morphology of Luanshibao Landslide in Tibetan Plateau. Q. J. Eng. Geol. Hydrogeol. 51, 13–16.
Grant, J.A., Wilson, S.A., Ruff, S.W., Golombek, M.P., Koestler, D.L., 2006. Distribution of rocks on the Gusev Plains and on Husband Hill, Mars. Geophys. Res. Lett. 33, 1258.
Hartley, A.J., Chong, G., Houston, J., Mather, A.E., 2005. 150 million years of climatic stability: evidence from the Atacama Desert, northern Chile. J. Geol. Soc. 162, 421–424.
Küppers, M., Jolliff, B.L., Nakamura, A.M., 2014. Boulder Field. In: Hargitai, H., Kereszturi, Á (Eds.), Encyclopedia of Planetary Landforms. Springer, New York, New York, NY, pp. 1–9.
Levy, J.S., Head, J.W., Marchant, D.R., 2008. Origin and Arrangement of Boulders on the Martian Northern Plains: Assessment of Emplacement and Modification Environments., pp. 39.
Levy, J.S., Fassett, C.I., Rader, L.X., King, I.R., Chaffey, P.M., Wagoner, C.M., Hanlon, A.E., Watters, J.L., Kreslavsky, M.A., Holt, J.W., Russell, A.T., Dyar, M.D., 2018. Distribution and characteristics of boulder halos at high latitudes on mars: ground ice and surface processes drive surface reworking. J. Geophys. Res. Planets 123, 322–334.
Maouche, S., Morhange, C., Meghraoui, M., 2009. Large boulder accumulation on the Algerian coast evidence tsunami events in the western Mediterranean. Mar. Geol. 262, 96–104.
Matmon, A., Quade, J., Placzek, C., Fink, D., Copeland, A., Neilson, J.W., Arnold, M., Aumaître, G., Bourlès, D., Keddadouche, K., 2015. Seismic origin of the Atacama Desert boulder fields. Geomorphology 231, 28–39.
McKay, C.P., Friedmann, E.I., Gómez-Silva, B., Cáceres-Villanueva, L., Andersen, D.T., Landheim, R., 2003. Temperature and moisture conditions for life in the extreme arid region of the Atacama desert: four years of observations including the El Niño of 1997-1998. Astrobiology 3, 393–406.
Mellon, M.T., Arvidson, R.E., Marlow, J.J., Phillips, R.J., Asphaug, E., 2008. Periglacial landforms at the Phoenix landing site and the northern plains of Mars. J. Geophys. Res. 113, 8599.
NASA/JPL/University of Arizona, 2011. Contact between Bouldery and Smooth Terrains. Image. https://www.uahirise.org/ESP_024117_1185.
Orloff, T.C., Kreslavsky, M.A., Asphaug, E.I., 2013. Possible mechanism of boulder clustering on Mars. Icarus 225, 992–999.
Placzek, C., Granger, D.E., Matmon, A., Quade, J., Ryb, U., 2014. Geomorphic process rates in the central Atacama Desert, Chile: Insights from cosmogenic nuclides and implications for the onset of hyperaridity. Am. J. Sci. 314, 1462–1512.
QGIS Development Team, 2019. QGIS Geographic Information System. Open Source Geospatial Foundation Project.
Quade, J., Reiners, P., Placzek, C., Matmon, A., Pepper, M., Ojha, L., Murray, K., 2012. Seismicity and the strange rubbing boulders of the Atacama Desert, northern Chile. Geology 40, 851–854.
Rosato, A., Strandburg, K.J., Prinz, F., Swendsen, R., 1987. Why the Brazil nuts are on top: Size segregation of particulate matter by shaking. Phys. Rev. Lett. 58, 1038–1040.
Rose, J., 1992. Boulder clusters in glacial flutes. Geomorphology 6, 51–58.
Rundel, P., Dillon, M., Palma, B., Mooney, H., Gulmon, S.L., Ehleringer, J., 1991. The phytogeography and ecology of the coastal Atacama and Peruvian Deserts. Aliso, 13.

Schindelin, J., Arganda-Carreras, I., Frise, E., Kaynig, V., Longair, M., Pietzsch, T., Preibisch, S., Rueden, C., Saalfeld, S., Schmid, B., Tinevez, J.-Y., White, D.J., Hartenstein, V., Eliceiri, K., Tomancak, P., Cardona, A., 2012. Fiji: an open-source platform for biological-image analysis. Nat. Methods 9, 676–682.

Wagner, T., Eglinger, J., 2017. Thorstenwagner/Ij-Ellipsesplit: Ellipsesplit 0.6.0 Snapshot. Zenodo.

Warren-Rhodes, K.A., Lee, K.C., Archer, S.D.J., Cabrol, N., Ng-Boyle, L., Wettergreen, D., Zacny, K., Pointing, S.B., 2019. Subsurface Microbial Habitats in an Extreme Desert Mars-Analog Environment. Front. Microbiol. 10, 69.

Westoby, M.J., Brasington, J., Glasser, N.F., Hambrey, M.J., Reynolds, J.M., 2012. Structure-from-Motion' photogrammetry: A low-cost, effective tool for geoscience applications. Geomorphology 179, 300–314.

Yong Technology Inc, 2014. GeoRose, Edmonton, Canada.